Quantifying the impacts of the angle of attack on the morphology of atmospheric von Kármán vortex streets

Stefano Annis[1], Maria Grazia Badas[1], Akos Horvath[2], and Sukanta Basu[3]

[1]Università degli Studi di Cagliari
[2]University of Hamburg
[3]University at Albany

July 31, 2023

Quantifying the impacts of the angle of attack on the morphology of atmospheric von Kármán vortex streets

Stefano Annis[1], Maria Grazia Badas[1], Ákos Horváth[2], Sukanta Basu[3,4]

[1]DICAAR, Università di Cagliari, Cagliari, Italy
[2]Meteorological Institute, Universität Hamburg, Hamburg, Germany
[3]Atmospheric Sciences Research Center, University at Albany, Albany, USA
[4]Department of Environmental and Sustainable Engineering, University at Albany, Albany, USA

Key Points:

- The mesoscale WRF model is used to study the characteristics of atmospheric von Kármán vortex streets (AVKVS) behind an elongated island.
- We have convincingly demonstrated that the wake asymmetry of an AVKVS decreases with increasing angle of attack.
- The wake asymmetry is fundamentally between trailing-edge and leading-edge eddies rather than between cyclonic and anticyclonic eddies.

Corresponding author: Maria Grazia Badas, `mgbadas@unica.it`

Abstract

A mesoscale model is used to systematically investigate how the incoming flow incidence angle affects the development of atmospheric von Kármán vortex streets for non-axisymmetric islands. The analysis is focused on an event observed on the leeward side of Guadalupe Island. By keeping the synoptic conditions the same, several simulations are performed for rotated orientations of the island topography, which correspond to a change in the angle of attack relative to the upstream flow. The asymmetry of the vortex shedding and the role of the leading and trailing edge are in line with what was observed in laboratory von Kármán vortex streets past a flat plate. The eddies become larger with increasing angle of attack while the shedding frequency decreases, and the asymmetry between cyclonic and anticyclonic eddies weakens. Cyclonic vortices are more developed and stronger under typical conditions when they are shed from the trailing edge. We also demonstrate that the wake asymmetry is fundamentally between trailing-edge and leading-edge eddies rather than between cyclonic and anticyclonic eddies.

Plain Language Summary

Low-level marine clouds in satellite images often reveal vortex streets formed by two rows of counter-rotating vortices on the leeward side of isolated mountainous islands. This phenomenon is called the "atmospheric von Kármán vortex street" (AVKVS) and has been investigated by satellite observations, laboratory experiments, and numerical modeling. Past studies highlighted an asymmetry between clockwise and counterclockwise rotating vortices, which was attributed to elongated island shapes and the effect of the Coriolis force. However, the origin of the AVKVS asymmetry is not yet fully understood. We use a mesoscale model to evaluate the effect of the incoming flow incidence angle (or angle of attack) on vortex street morphology for an elongated island. We first realistically simulate a vortex street observed downstream of Guadalupe Island and then, by keeping the same meteorological conditions, we simulate the phenomenon with artificially rotated island orientations to modify the angle of attack. The results show that the dimension of the vortices increases but their asymmetry weakens with increasing angle of attack. We also demonstrate that the wake asymmetry is fundamentally between trailing-edge and leading-edge eddies rather than between cyclonic and anticyclonic eddies.

1 Introduction

The atmospheric von Kármán vortex street (AVKVS) is a classic wake flow pattern in the lee of mountainous islands: it comprises two rows of counter-rotating vortices made visible by low-level clouds. This phenomenon, which was initially observed and studied from satellite images (Hubert & Krueger, 1962; Chopra & Hubert, 1965), arises in the presence of a well-mixed boundary layer with an inversion below the peak of the island (Etling, 1989) and winds with almost steady direction (Heinze et al., 2012). AVKVS has strong similarities with the simpler von Kármán vortex street (VKVS) observed in laboratory bluff body flows (Kármán, 1911; Karmán, 1912), although in atmosphere the phenomenon is characterized by more complex conditions due to fluid stratification, flow unsteadiness, and the irregular geometry of the obstacle.

An early laboratory experiment by Fage et al. (1927) on the VKVS behind an inclined flat plate showed that the features of the vortex street are affected by the angle between the incoming flow and the long axis of the plate, hereafter referred to as the angle of attack (or AoA). More recently, the laboratory experiments of Lam (1996) and Lam and Leung (2005) on vortex shedding behind an inclined flat plate at different angles of attack highlighted an asymmetric wake, with cyclonic vortices shed from the trailing edge being stronger than anticyclonic ones originating from the leading edge. The same be-

havior also emerged in numerical simulations of flat plate flows (Breuer & Jovičić, 2001; Lam & Wei, 2010; Yang et al., 2012). This asymmetry was explained with different formation mechanisms for the two trains of vortices. Trailing-edge vortices simply roll up and are directly shed into the flow without being affected by the obstacle. In contrast, leading-edge vortices initially remain attached to the obstacle and are then detached as fully-fledged vortices by the growth of the next trailing-edge vortex. Thus, leading-edge vortices are also shed into the wake at an axial location near the trailing edge. As a result, the asymmetry arises because the leading-edge vortices undergo a more prolonged birth before detachment and are more diffused with a smaller peak vorticity than trailing-edge vortices at the same axial location.

Asymmetry was also detected in the analysis of AVKVS. An LES simulation performed by Heinze et al. (2012) in the wake of an idealized Gaussian-shape island revealed stronger cyclonic vortices than anticyclonic ones. This asymmetry was attributed to the effect of the Coriolis force, which in the northern hemisphere weakens the anticyclonic vortices and reinforces cyclonic ones.

Ágústsson and Ólafsson (2014) discussed an asymmetric AVKVS downstream Mt. Snæfellsjökull in West Iceland, which was observed by Moderate Resolution Imaging Spectroradiometer (MODIS) satellite images. They attributed this behaviour to the asymmetry of the mountain and to the presence of lower topographic disturbances limiting the shedding of anticyclonic vortices. Cyclonic-anticyclonic asymmetry also emerged in the images of other satellite studies (Etling, 1990); however the spatiotemporal resolution of wind retrievals was too coarse to resolve small-scale wake flows; hence, the analysis was limited to a visual inspection.

Afterwards, Horváth et al. (2020) and Günther et al. (2021) used a time series of Geostationary Operational Environmental Satellite-R (GOES-R) winds to investigate the evolution of the AVKVS in the lee of Guadalupe Island on 9 May 2018. These latest observational studies highlighted an asymmetry in the vorticity decay of cyclonic and anticyclonic vortices, which was attributed to the effect of Earth's rotation and the non-axisymmetric shape of the island.

Different features can be identified in the AVKVS occurring on the leeward side of Guadalupe island. Figure 1 shows satellite images of four different vortex streets recorded by MODIS Terra and Aqua (NASA Worldview, https://worldview.earthdata.nasa.gov). Panel (a) depicts the AVKVS observed on 5 July 2021, whose wake is aligned along the North-South direction. Panel (b) is the AVKVS analyzed by Horváth et al. (2020), featuring a wake in the southeast direction. The panel (c) event occurred on 20 June 2021, when the upstream flow was more westerly, and the vortex street development was limited by the proximity of the California coast. Finally, in panel (d) the case of 17 June 2021 shows a vortex street in the northeast direction, which was even more constrained by the presence of the coast. The images reveal differences among the vortex streets not only in the propagation direction, but also in the size and asymmetry of cyclonic and anticyclonic vortices. The coherent structures in panel (c) are larger than in panel (a) and (b), while the apparent differences between cyclonic and anticyclonic vortices are smaller. In panel (d), fewer vortices are visible than in the other three cases, although their size is bigger.

Because the different AVKVS portrayed in Figure 1 occurred at the same location, the Coriolis term is the same. Hence, the observed differences in vortex asymmetry must be largely due to the variation in the upstream wind direction, and thus the angle of attack.

While many studies are devoted to analyzing the effect of the angle of attack on the asymmetry of laboratory VKVS, a similar analysis for the atmospheric counterpart has not been performed yet. We thereby present a systematic mesoscale modeling work to investigate this issue. In the current study, the AVKVS described by Horváth et al. (2020) is simulated as a control case, which is then compared with model runs that use vari-
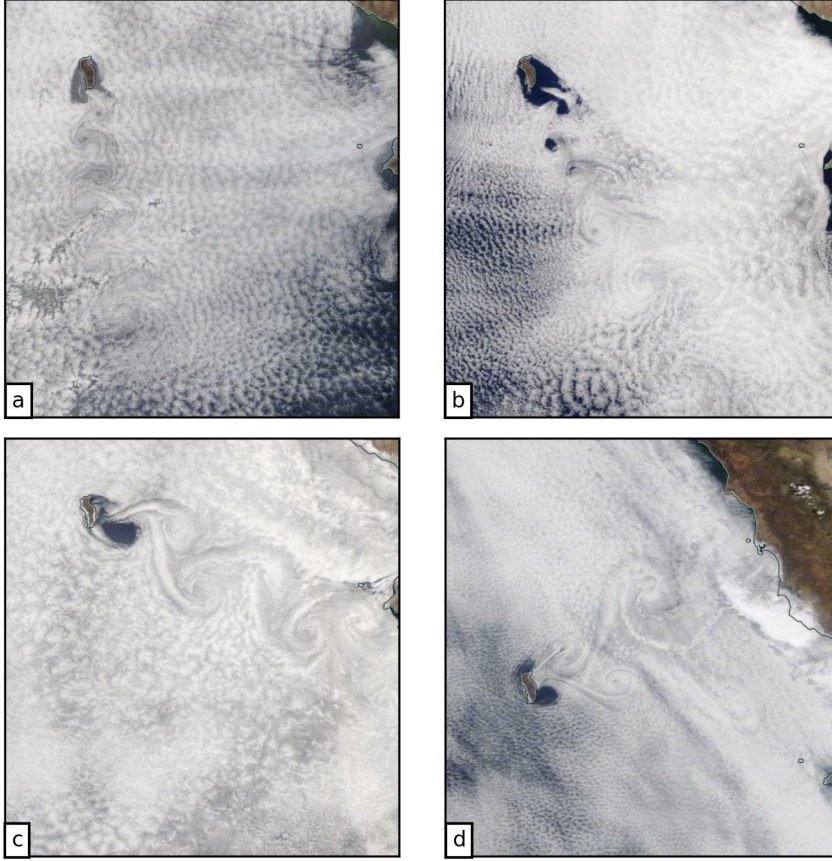
Figure 1. Satellite images of three different von Kármán vortex streets in Guadalupe's wake: (a) 5 July 2021, MODIS-Terra, (b) 9 May 2018, MODIS-Terra, (c) 20 June 2021, MODIS-Aqua and (d) 17 June 2021, MODIS-Terra.

ous rotated orientations of Guadalupe's topography to investigate the sensitivity of vortex formation and evolution to the angle of attack. This approach ensures that simulations are performed under realistic atmospheric conditions and, at the same time, avoids the geographically limiting effect of the nearby California coast on AVKVS development, which would arise if the upstream wind direction were modified instead of changing island orientation.

The feasibility of simulating AVKVS under realistic conditions by means of mesoscale models has already been demonstrated. For example, X. Li et al. (2008) simulated the wake in the lee of the Aleutian Islands (Alaska) with the MM5 model obtaining similar wind patterns to those obtained from SAR (Synthetic Aperture Radar) retrievals.

Several authors concentrated their efforts on simulating observed AVKVS with the Weather Research and Forecasting (WRF) model. Among them, Couvelard et al. (2012) showed that the model is able to reproduce the wakes in the lee of Madeira Island realistically. Caldeira and Tomé (2013) pointed out that an increase in sea surface temperature (SST) may change the regime from vortex-shedding to a long straight wake. Nunalee and Basu (2014) using real as well as idealized island topography assessed how the island diameter at the planetary boundary layer (PBL) inversion height is the dominant length scale associated with the AVKVS shedding frequency. Nunalee, He, et al. (2015) studied the

impact of the AVKVS on optical ray trajectories using different test cases (including Madeira, Guadalupe, Hawai wakes). Nunalee, Horváth, and Basu (2015), using a DEM with different resolutions, demonstrated that the correct representation of the topography is crucial to correctly reproducing AVKVS by high-resolution mesoscale models. Grubišić et al. (2015) performed a sensitivity analysis of the vortex street formation to surface friction and thermal forcing. Ito and Niino (2016) successfully simulated an AVKVS observed in the lee of Jeju Island (South Korea) and investigated the vortex formation mechanism using the Japanese Meteorological Agency non-hydrostatic mesoscale model.

Recently, Gao et al. (2023) performed a 10-year simulation of Madeira vortex streets with the COSMO model to assess the dependency of vortex shedding on the synoptic flow conditions. They also developed a vortex identification algorithm, leading to a favorable comparison among simulations and remotely-sensed observational data.

The paper is organized as follows. Section 2 describes the WRF model set-up that proved adequate to reproduce the observed AVKVS, as described in Section 3. Results obtained for simulations performed under different orientations of Guadalupe island are presented in Section 4 to shed light on the sensitivity of vortex shedding to the angle of attack, the importance of the leading and trailing edge, as well as their effect on the cyclonic-anticyclonic asymmetry and vorticity decay. Finally, Section 5 summarizes our results and provides an outlook on future research aimed at unveiling the physics behind these beautiful wake patterns.

2 Methodology

2.1 Dimensionless Numbers

For the characterization of the vortex street, three different dimensionless numbers are used: the Reynolds number (Re), the Froude number (Fr), and the Strouhal number (St). The Reynolds number is computed as:

$$Re = \frac{u_0 \cdot D}{\nu} \tag{1}$$

where u_0 is the upstream wind speed, ν is the kinematic viscosity and, following Horváth et al. (2020), D is a characteristic length of the obstacle, which is here the minor axis of the "mass density" ellipse fitted to Guadalupe Island (plotted in Figure 2a).

Atmospheric flows are dominated by turbulent diffusion; thus, a modified Reynolds number, Re_k, can be defined by using the eddy viscosity, K_M, in place of the kinematic one, as suggested by Nunalee and Basu (2014). Here, the eddy viscosity given by the WRF model was volume averaged within the boundary layer upstream the island to compute Re_k.

The Froude number is computed with the equation:

$$Fr = 1 - \frac{h_c}{h_i} \tag{2}$$

where h_c is the dividing streamline defined by Snyder et al. (1985) and h_i is the peak height of the island ($h_i = 1188\ m$). The dividing streamline height, h_c, can be considered a critical height: the air parcels below this height go around the obstacle, while those moving above this height go over the obstacle. The Froude number was computed following Heinze et al. (2012): the dividing streamline height is determined by iteratively solving the equation:

$$\frac{1}{2}u_0^2(h_c) = \int_{h_c}^{h_i} N^2(z)(h_i - z)dz \tag{3}$$

where u_0 is the upstream wind speed, and N is the Brunt-Väisälä frequency:

$$N = \sqrt{\frac{g}{\theta_0}\frac{\partial\bar{\theta}}{\partial z}} \tag{4}$$

where g is the gravitational acceleration, θ_0 is a reference potential temperature and $\frac{\partial\bar{\theta}}{\partial z}$ is the upwind potential temperature profile.

The normalized vortex shedding frequency is represented by the Strouhal number, which is computed as:

$$St = \frac{d'}{T \cdot u_0} \tag{5}$$

where d' is the crosswind island diameter at the mean inversion height, u_0 is the upstream velocity, and T is the mean shedding period between two like-rotating vortices.

Another dimensionless number that characterizes vortex streets in the presence of rotation is the Rossby number, Ro, defined as the ratio of inertial to Coriolis forces. However, since Coriolis only depends on the rate of Earth's rotation and latitude, and synoptic forcing is the same for all the simulations, the Ro value is identical for all the runs.

2.2 WRF numerical set-up

We used the Weather Research and Forecasting (WRF) model (version 3.9.1.1), a regional non-hydrostatic atmospheric simulation system (Skamarock et al., 2008), to investigate the role of the angle of attack on AVKVS formation. Even though it is possible to perform large-eddy simulations with the WRF model, it is primarily used in practice as a Reynolds-Averaged Navier-Stokes (RANS) solver. For the RANS simulations, the horizontal grid spacing is larger than the largest energy-containing eddies of the boundary layer, and all scales of turbulence are parameterized. In the vertical direction, turbulent fluxes are modeled using one-dimensional planetary boundary layer (PBL) parameterizations. In this study, the level 2.5 Mellor-Yamada-Nakanishi-Niino (MYNN2) closure scheme (Nakanishi & Niino, 2004) is adopted. In the horizontal plane, a simple diffusion scheme by Smagorinsky is used. The revised MM5 Monin-Obukhov (Jiménez et al., 2012) scheme was used for the surface layer, while the NOAH scheme (Chen & Dudhia, 2001) was adopted as land surface model. Moreover, we adopted the WRF single moment five-class microphysics scheme (Hong et al., 2004). In addition, the RRTMG (rapid radiative transfer model for general circulation models) scheme (Iacono et al., 2008) was used for both shortwave and longwave radiation parameterizations. For cumulus parameterization, the multi-scale Kain–Fritsch scheme (Kain, 2004) was activated only in the outer domain. This set of physical parameterization schemes was chosen to allow an adequate reproduction of the observed control case (see Section 4). The initial and lateral boundary forcings were taken from the ERA5 reanalysis (Hersbach et al., 2020) at 1-hr intervals. The set-up consists of 56 vertical pressure levels from the surface to 10 hPa (with 23 levels below 1 km) using 1-way nesting.

The island has a steep topography and an elongated shape with a width-to-length ratio of approximately 1/3, as apparent from Figure 2a. The island has a complex shape, and it is not exactly symmetric. However, for simplicity, we have fitted the "mass density" ellipse, which leads to considerable variations in crosswind island diameter as a function of upstream wind direction and also defines a leading and trailing edge relative to

the upstream flow (Horváth et al., 2020). Both of these factors play a fundamental role in vortex structure development.

The three nested domains having a grid spacing of 9/3/1 km respectively are shown in Figure 2b, with corresponding details given in Table 1. Since the correct reproduction of orography is crucial to correctly simulate AVKVS (Nunalee, Horváth, & Basu, 2015), the default 30 arc-seconds GMTED2010 (Global Multi-resolution Terrain Elevation Data 2010, Danielson and Gesch (2011)) was replaced with its 7.5 arc-seconds resolution version. This DEM, with a spatial resolution of about 225 m, was resampled to the resolution of the model grid in the WRF Pre-Processing System (WPS), which decreased the peak height by about 6% in the innermost d03 domain (whose resolution is 1km).
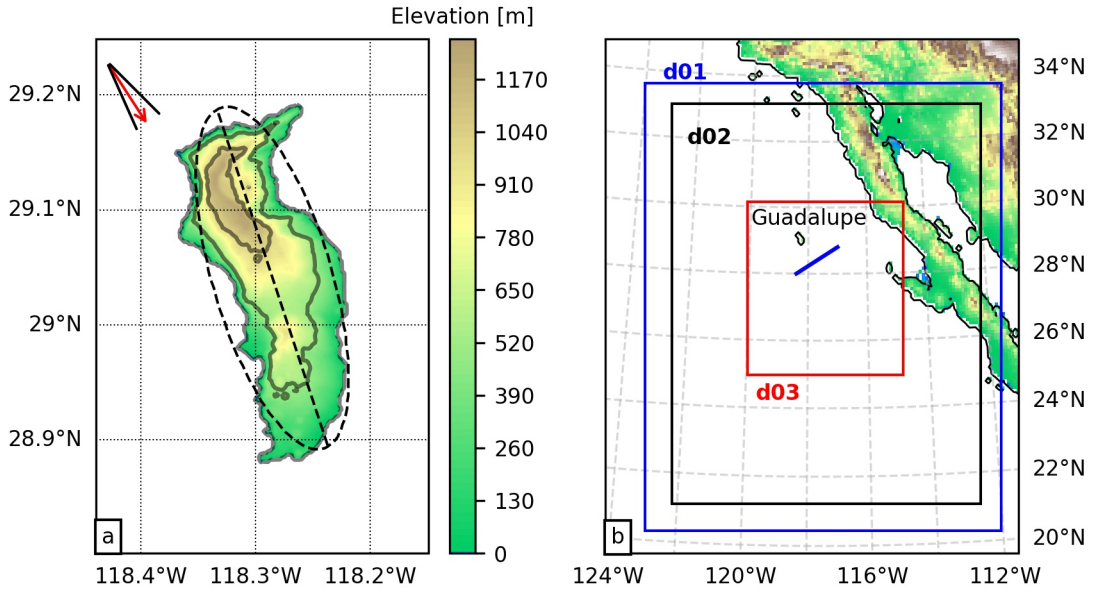
Figure 2. Topography of Guadalupe island. The Global Multi-resolution Terrain Elevation Data 2010 (GMTED2010) at 7.5 arc-seconds was used, and the dashed lines represent the fitted "mass density" ellipse and its major axis. The two black segments identify the range of the wind directions during the observed event, while the red arrow indicates the mean direction (panel a). The three nested domains used for the WRF simulations; the cross-section downstream the island was used for the Hövmoller diagrams (panel b).

The WRF simulations started at 20:00 UTC on 8 May 2018 and finished at 23:00 UTC on 9 May 2018, for a total of 27 hours. A spin-up of six hours was considered; hence, results were analysed from 02:00 UTC of 09 May 2018 onward. All analyses were performed in the d03 domain at 1 km grid spacing, which is large enough to allow the use of a mesoscale model, but small enough to correctly represent the vortices, whose diameter is approximately 20-40 km (Etling, 1989).

3 Results: Reference Case

In order to use the WRF model as a numerical laboratory for testing the influence of wind incidence angle on vortex street development, the model's ability to reproduce AVKVS was first confirmed by simulating the case described by Horváth et al. (2020) (see Figure 1b). This atmospheric von Kármán vortex street occurred on 9 May 2018 (Section

Domain	Δx, Δy [km]	Δt [s]	Nx	Ny	Dimensions $[km^2]$
d01	9	25	133	167	1188×1494
d02	3	5	346	448	1035×1341
d03	1	1	523	580	522×579

Table 1. Domain configurations

1). The hourly evolution of vertical profiles computed upstream the island and shown in Figure 3, depicts typical conditions favoring the onset of AVKVS. The inversion height of the potential temperature profile (panel a) increases during the day (the island is in a timezone of UTC-7), but it is always lower than the peak height of the island (approximately 1188 m), as required for the formation of the AVKVS (see section 1). Panel b portrays the typical boundary layer wind speed profiles, where the upper-level wind is more variable in the morning hours. As expected, the eddy viscosity profiles (panel c) display a maximum within the boundary layer and zero values above.
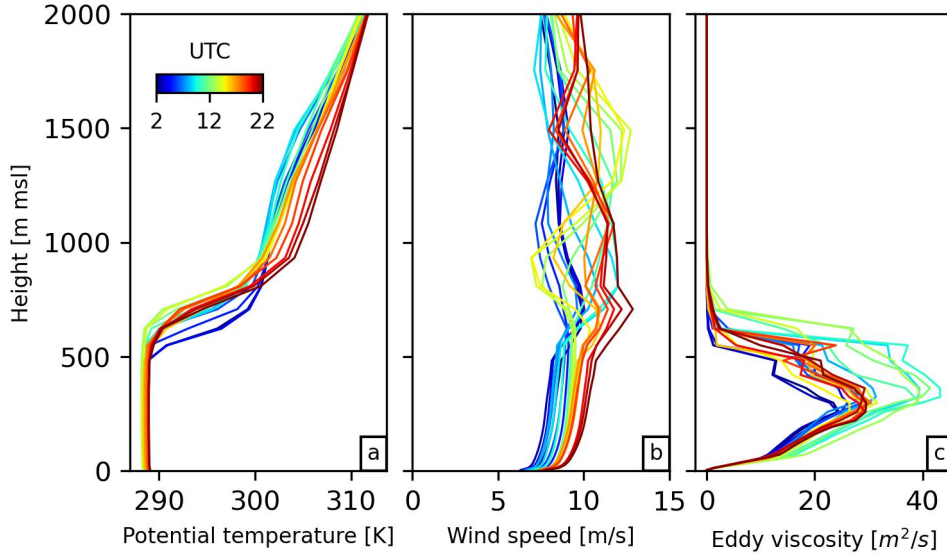

Figure 3. Vertical profiles of potential temperature (panel a), wind speed (panel b) and eddy viscosity (panel c). The plot shows hourly averages from 2:00 UTC to 22:00 UTC on 9 May 2018 with different colors.

Figure 4 shows a volume rendering of the simulated vertical component of relative vorticity up to 750 m (MSL) and superimposed on the MODIS-Terra satellite image retrieved at 18:12 UTC on 9 May 2018. The comparison shows that the simulation is generally consistent with the satellite image.

Horváth et al. (2020) using a satellite-derived wind dataset noted unsteady upstream wind speed and direction, which resulted in a varying angle of attack α between 9° and 32°. Figure 5 compares the time evolution of the wind speed and its two components (along West-East and South-North directions) at two locations, one inside and one outside the wake, as derived from satellite data and obtained from WRF simulation. Despite some differences due to wind retrieval uncertainties and different spatial resolutions (satellite
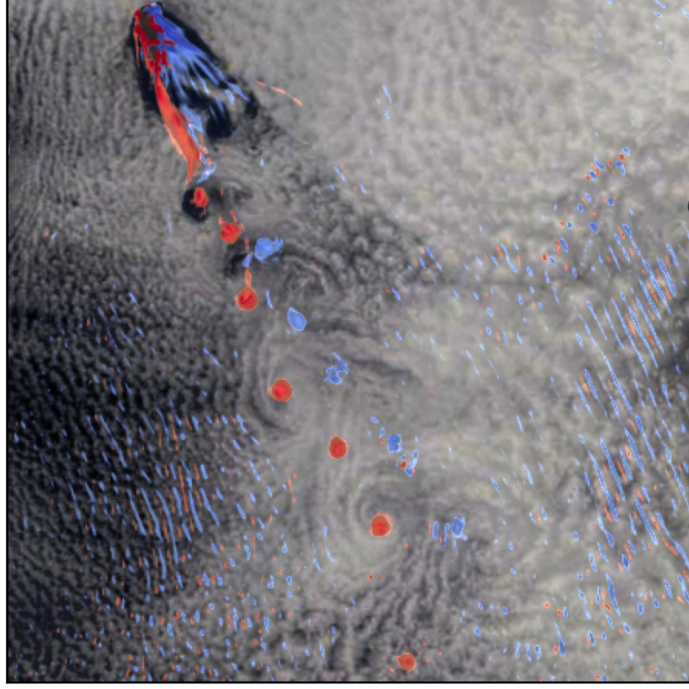
Figure 4. Vorticity volume rendering from the control run is superimposed on the MODIS-Terra satellite image captured at 18:12 UTC on 9 May 2018. Cyclonic/anticyclonic vortices are displayed in red/blue colors respectively. The image was obtained by means of the Vapor software (S. Li et al., 2019)

data were reconstructed on a 3km grid), the temporal evolution of the simulated winds closely resembles the observed one.

As described by Horváth et al. (2020), the upstream wind had a considerable westerly turn between 15–17 UTC and then swung back, which resulted in the easterly shift of earlier-shed vortices in the far wake and even led to the eventual merger of two consecutive anticyclonic vortices. The enhanced cross-street flow and the directional swings observed by satellite data were less marked in the numerical results derived from smooth ERA5 winds (Figure 5), which may largely explain the differences between the locations of the simulated and observed vortex cores visible in Figure 4. Moreover, as seen in Figure 5a, the simulated wind speed from about 18:00 onwards is smaller than the one from GOES-16. This behavior is consistent with Figure 4, where the simulation shows more vortices than the satellite images. Because the simulated wind velocity inside the wake (and hence the propagation speed of the vortices) is smaller than the observations, the modelled vortices persist in the wake for a longer time and thus their number is higher at a fixed time. Despite such differences, the results obtained are generally consistent with the satellite data and the vortex street asymmetry highlighted by Horváth et al. (2020) emerges in the simulations too.

The favorable comparison between observations and simulations confirms that the model, with the numerical set-up described in Section 2, is able to reproduce the onset and evolution of the AVKVS with reasonable accuracy. Henceforth, this particular simulation is referred to as the control case (CC).
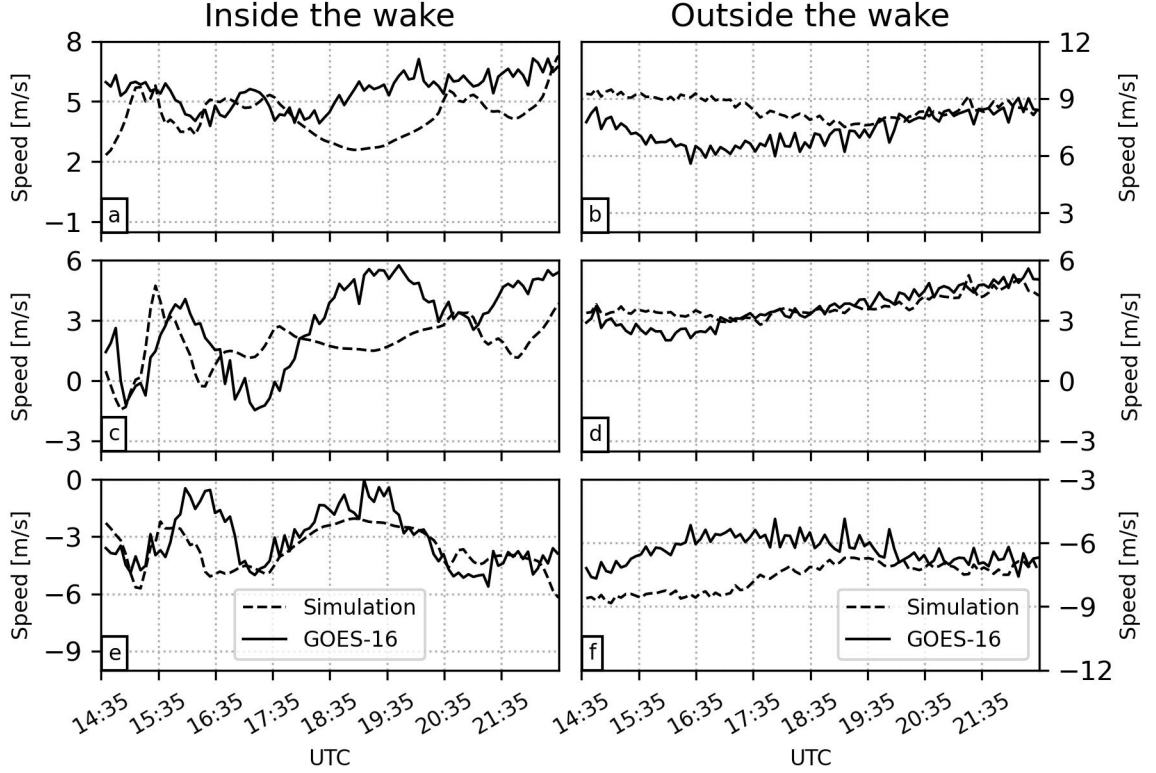
Figure 5. Temporal variation of wind speed (panels a and b) and E-W (panels c and d) and N-S (panels e and f) wind components inside (left side) and outside (right side) Guadalupe's wake as retrieved by GOES-16 (data from Horváth et al. (2020)) and simulated in the control run.

4 Results: Sensitivity Analysis

4.1 Sensitivity to the angle of attack

The angle of attack, α, is defined here as the difference between the mean upstream wind direction (327.1°) and the orientation of the major axis of the "mass density" ellipse fitted to the island. Following Horváth et al. (2020), the control case uses the true orientation of Guadalupe (ellipse major axis at 343.4°) and, thus, $\alpha = 16.3°$. For the sensitivity analysis, three rotated orientations were considered: the two extreme cases when the island is parallel with ($\alpha = 0°$) or orthogonal to ($\alpha = 90°$) the mean flow, and an intermediate case with $\alpha = 45°$. In order to obtain these three modified set-ups, the topography and the other relevant parameters related to the terrain (e.g. albedo, land use, leaf area index, etc.), were rotated by -16.3°, 28.7° and 73.7°, respectively, to obtain $\alpha = 0°, 45°, 90°$ (clockwise rotation is positive). The true and rotated topographies, as represented in the innermost domain (d03), are shown in Figure 6. Since we use the synoptic conditions of a real event, the upstream flow characteristics are unsteady, and hence the angle of attack varies somewhat during both the control case and the rotated ones. We also note that the modified configurations lead to a considerable change in the crosswind island diameter at the mean inversion height (d'). Specifically, d' increases with α for $\alpha \leq 90°$ so its value is respectively minimum and maximum for the two extreme orientations of $\alpha = 0°$ and $\alpha = 90°$. While for $\alpha = 45°$, it has an intermediate value (further details on the effect of d' on vortex formation are discussed in Section 4.3).

Figure 7 shows the vorticity map at the height of 350 m (MSL) at 13:00 UTC on 9 May for the four simulated cases. Although at this time only two of the configurations have a well-developed vortex street (the control case and $\alpha = 45°$), the differences in the size of the vortices are already apparent: the coherent structure dimensions increase with d', in agreement with findings for vortex streets behind a flat plate (Lam & Wei, 2010).
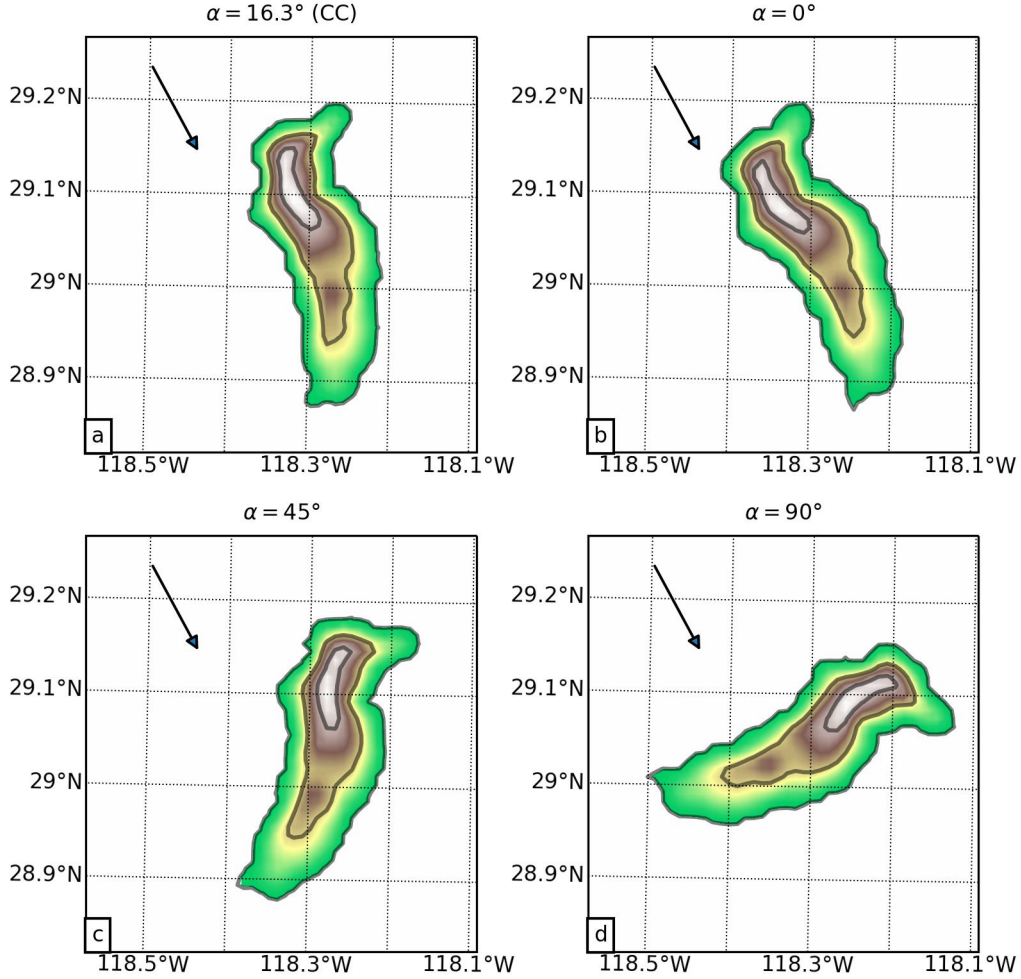

Figure 6. Topography of the innermost d03 domain for (a) the control case and (b, c, d) for the rotated orientations (angles displayed in the plots). The arrows indicate the average upstream wind direction.

Figure 8 depicts the Hövmoller diagrams computed along a cross-street section downstream of the island (plotted in Figure 2-b and Figure 7) for the four different simulations. The increase of the vortex size with the angle of attack (and consequently with d') is confirmed from this figure. Furthermore, the angle of attack controls the temporal evolution of vortex shedding, explaining the lack of a well-developed vortex street for the two extreme orientations at 13:00 UTC in Figure 7. By this time, vortex shedding is already finished for $\alpha = 0°$, while it has just started for $\alpha = 90°$.

As previously mentioned, satellite observations of our control case revealed an asymmetric vortex street. This asymmetry was successfully reproduced by the control simulation, which clearly shows larger, stronger, and more coherent footprints of cyclonic (positive)
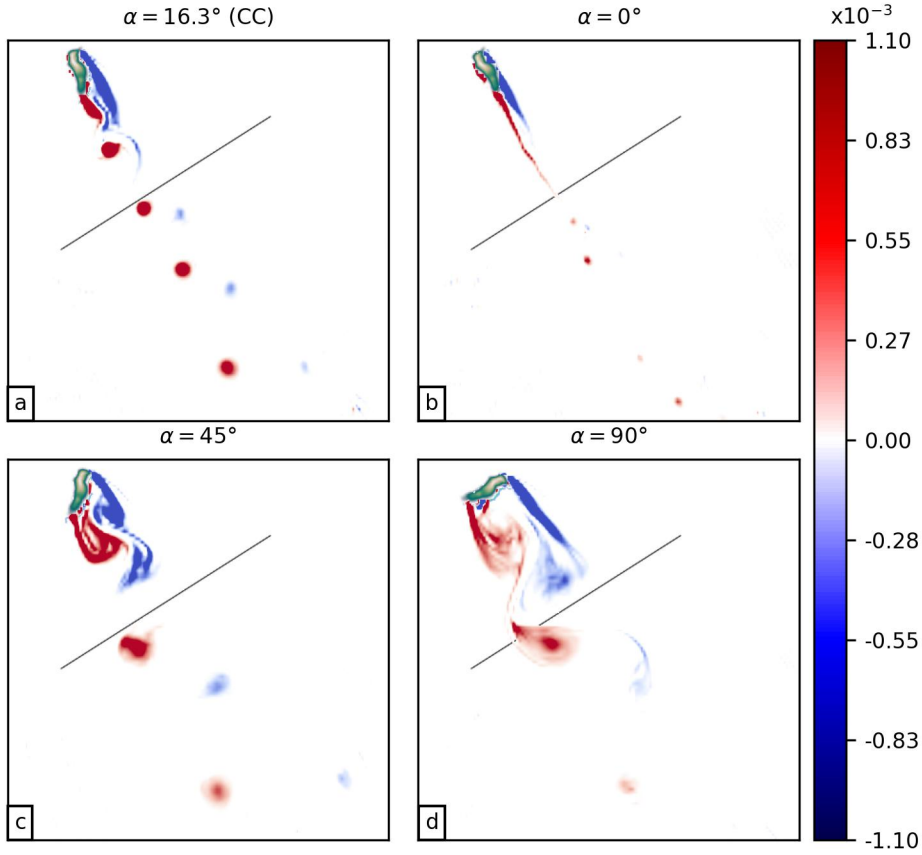
Figure 7. Horizontal slice of vorticity $[s^{-1}]$ at the height of 350 m (MSL) at 13:00 UTC on 9 May for (a) the control case and (b, c, d) the rotated island. The cross-section downstream of the island that was used for the Hövmoller diagrams (Figure 8) is also plotted.

vortices with respect to those belonging to anticyclonic (negative) ones (see Figure 8a). The Hövmoller diagrams also indicate that the asymmetry of the wake decreases with increasing angle of attack. When the island is parallel with the mean flow ($\alpha = 0°$), the wake appears to be quite different from the classic AVKVS consisting of counterrotating vortex pairs. Indeed, it is strongly asymmetric with seven cyclonic vortices, but only one well-formed anticyclonic vortex, and the former vortices have higher peak vorticity than the latter. For the control run, with an average angle of attack of 16.3°, the asymmetry is still present but weaker: there are now five anticyclonic vortices, and the difference in absolute peak vorticity is reduced. The case with $\alpha = 45°$ shows an equal number of positive and negative vortices, but positive absolute peak vorticities are still larger than negative ones. In contrast, when $\alpha = 90°$ the wake is practically symmetric, featuring an equal number of cyclonic and anticyclonic vortices and similar peak vorticities.

4.2 The role of the leading and trailing edges

In our numerical experiments, the control run shows cyclonic trailing-edge vortices that are not only stronger but also more coherent than the anticyclonic leading-edge ones. This asymmetry progressively becomes weaker for higher angles of attack, and when the island is perpendicular to the mean flow ($\alpha = 90°$), there is no meaningful distinction
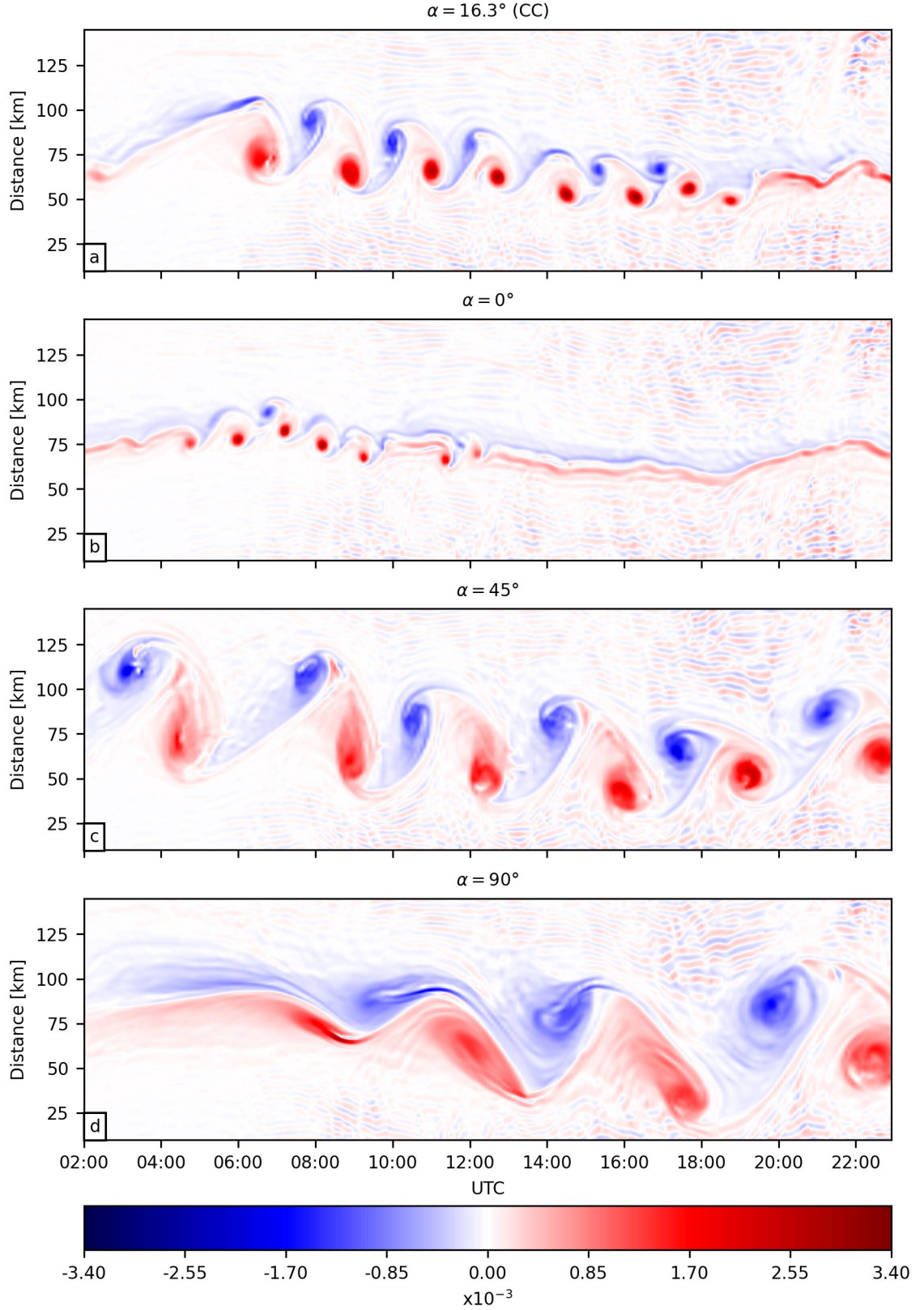
Figure 8. Hövmoller diagrams of vorticity $[s^{-1}]$ computed along the cross-street section indicated in Figure 2b and Figure 7 for the control case (panel a) and rotated orientations (panels b, c, d).

between a trailing or leading edge. The vortices are equally developed and symmetric (panel d in Figures 7 and 8).

In order to further demonstrate that the trailing edge sheds stronger vortices, another simulation with an angle of attack of -45° was performed. Under this configuration, the leading and trailing edges are swapped, and the northern and southern shores of the island generate vorticity of opposite signs compared to all previous configurations. Figure 9a shows the rotated topography for this case, and a horizontal slice of the simulated vorticity at the height of 350 m (MSL) is displayed in Figure 9b. Beside an eastward shift in the vortex street direction, the comparison of Figure 9b and Figure 7c shows that the cyclonic-anticyclonic asymmetry is reversed: in the $\alpha = -45°$ case the anticyclonic vortices are better developed and have stronger vorticity than the cyclonic ones.

These results point to an AVKVS behaviour similar to the one observed in laboratory and numerical studies of VKVS already exposed, where the wake flow is strongly dominated by the evolution and shedding of the trailing edge vortex.

The asymmetry is in fact between trailing-edge and leading-edge vortices rather than between cyclonic and anticyclonic vortices. The corresponding Hövmoller diagram is plotted in Figure 9c: the AVKVS has an equal number of positive and negative vortices, but here the anticyclonic (trailing-edge) vortices have higher peak vorticity than the cyclonic (leading-edge) ones.

As previously stated, the asymmetry for Guadalupe is minimum for $\alpha = 90°$ and increases with the decrease of the angle of attack, reaching its maximum for $\alpha = 0°$, when anticylonic vortices almost vanish. However, since $\alpha = -45°$ displays a switched asymmetry with stronger anticyclonic than cyclonic vorticies, we hypothesize that a small negative AoA might restore a symmetric vortex street, while for larger negative AoA asymmetry should increase, although favouring anticyclonic vortices. We also speculate that vortex streets for an idealized elliptic-shaped island should be symmetric concerning cyclonic and anticylconic vortices (neglecting Coriolis effects) for $\alpha = 0°$ and $90°$ and vortex asymmetry would then be maximum for some angle in between.

4.3 Coherent structures: vortex tracking, geometric features, and vorticity decay

In order to compare vortex street properties for the five different cases and characterize vortex street asymmetry, a vortex tracking algorithm was developed.

AVKVS eddies are pancake vortices with a large width-to-height aspect ratio and their structure is fairly constant along the vertical direction (Heinze et al., 2012). Hence, their identification is straightforward in 2D horizontal slices. We compared using vorticity, potential temperature, and Okubo–Weiss criteria for vortex identification, which lead to similar results, but out-of-plane vorticity proved to be more persistent. Hence, our algorithm works on a horizontal slice of vorticity at a fixed height (350 m above sea level) as input and implements the following criteria to identify vortices and remove background noise:

1. Consider only a limited area downstream of the island (black dotted rectangle in Figure 10);
2. The vortex must be fully within the rectangle;
3. Absolute value of relative vorticity $\geq 4 \cdot 10^{-4}\ s^{-1}$;
4. Minimum vortex area of 50 km^2 for all the simulations except for the case with $\alpha = 0°$ where a threshold of 25 km^2 was adopted;
5. Maximum vortex eccentricity of 0.98;
6. Limiting condition on the position of the new vortices (which have to be shed near the upper boundary of the rectangle), and on the distance between the centroid
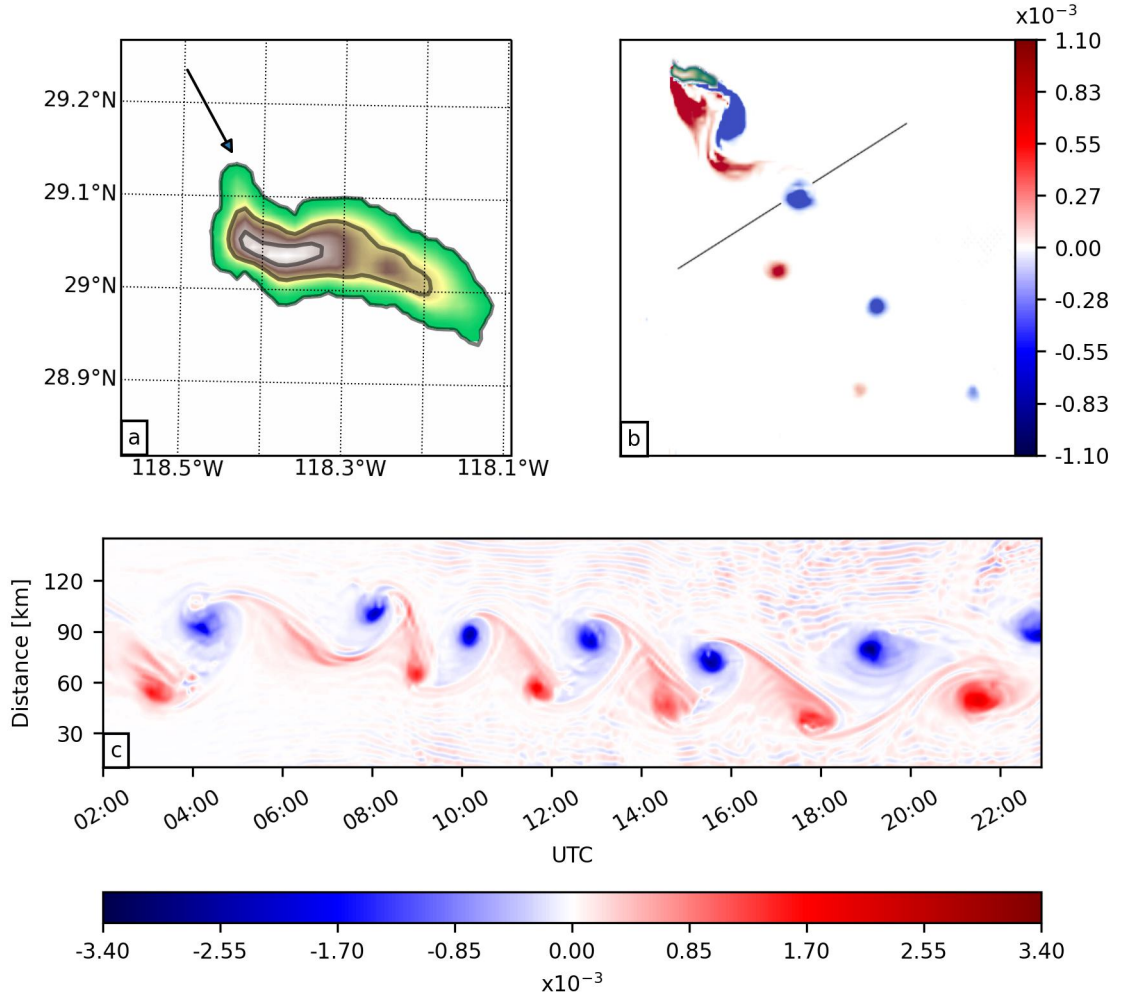
Figure 9. Topography for the case with α = -45° in the d03 domain, the arrow indicates the mean wind direction (panel a). For the same simulation: horizontal slice of vorticity $[s^{-1}]$ at the height of 350 m (MSL) at 13:00 UTC on 9 May 2018 (panel b), and Hövmoller diagram of vorticity $[s^{-1}]$ (panel c) computed along the cross-section plotted in panel b.

of the same vortex over time (i.e. vortices move downstream, with an advection velocity comparable to the upstream wind speed).

Some of the above criteria are similar to those adopted by Gao et al. (2023). Data were analyzed with a time-step of fifteen minutes. A snapshot of vortex identification and tracking for two of the analyzed simulations is displayed in Figure 10. The plot also shows how the geometric properties of the vortex street are derived from vortex triplets: a is the streamwise distance between two like-rotating vortices, h is the transverse distance between the two rows of vortices, which allows computing the triplet aspect ratio h/a and the dimensionless width h/d', normalized by the obstacle crosswind diameter at the mean inversion height d'.

The identification of the vortices also allowed the calculation of the Strouhal number (see equation 5), where the mean shedding period is derived from the tracked triplets (Heinze et al., 2012) as:
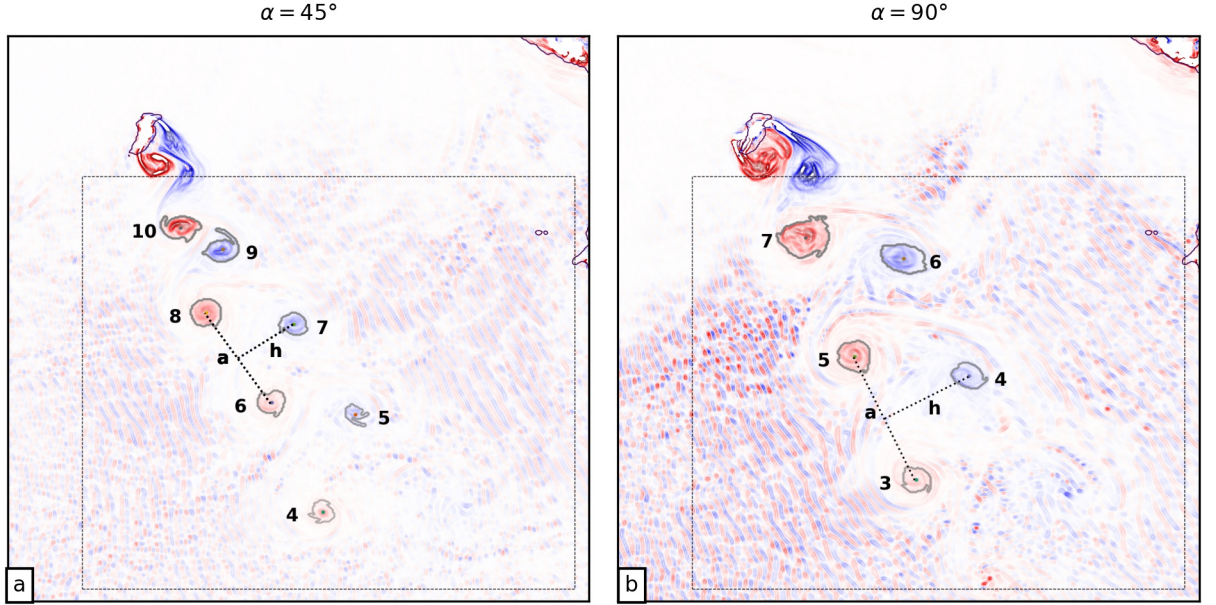
Figure 10. Example of vortex identification and tracking for two of the analyzed cases. The colormaps represent a horizontal slice of vorticity at the height of 350 m (MSL). The dotted box defines the area where vortices are tracked. Identified coherent structures are numbered, and their boundaries are marked by grey contours. The derived geometrical features of a triplet are the streamwise distance between two like-rotating vortices, a, and the transverse distance between the two rows of vortices, h.

$$\overline{T} = \overline{a}/\overline{u_e} \qquad (6)$$

where $\overline{a}$ is the time-averaged distance between two consecutive like-rotating vortices, and $\overline{u_e}$ is the mean propagation speed of the vortices. We computed $\overline{T}$ for each triplet and then considered its mean value over all triplets. Due to the unsteadiness of the incident flow, average values are also considered for u_0 and d'_{inv} (eq. 5).

For comparison, the Strouhal number was also computed by deriving shedding frequency from the time history of positive and negative peak vorticity along the transect used for the Hövmoller diagrams (Figures 8 and 9c). Specifically, the mean shedding period was calculated as the average time interval between two consecutive vortices of the same sign (Figure 11). The derived geometrical parameters and Strouhal numbers are given in Table 2.

Notwithstanding differences in the T values obtained with the two methods, the shedding period appears to be an increasing function of d'. For the observed control case, the mean aspect ratio h/a obtained from the WRF simulation (0.42) closely matches the values obtained by Horváth et al. (2020) by analyzing satellite images of triplets less affected by the wind unsteadiness (0.42-0.46). Moreover, average geometrical features obtained in the different model configurations are consistent with those reported by Young and Zawislak (2006), who studied the geometric characteristics of 30 different vortex streets in MODIS images. The simulated triplets have an aspect ratio, h/a, ranging from 0.34 to 0.53, while the 95% confidence interval found by Young and Zawislak (2006) has a minimum of 0.36 and a maximum of 0.47. The dimensionless widths h/d' are in the range
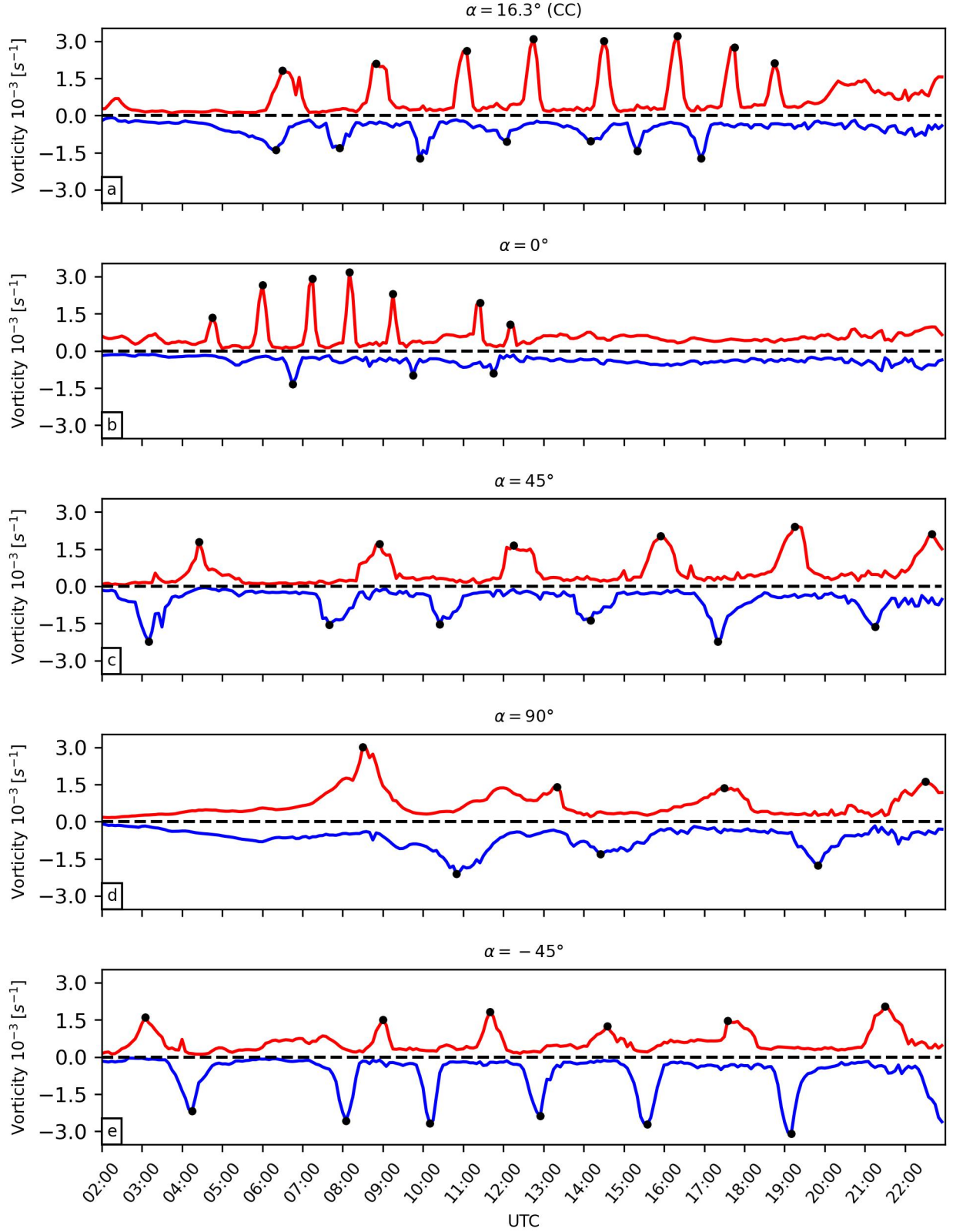
Figure 11. Maxima (red) and minima (blue) of vorticity computed along the section marked in Figure 2b and Figure 7 versus time for the control case (panel a) and the island rotations corresponding to $\alpha =$ to 0°, 45°, 90°, -45° (panel b, c, d, e respectively). The black points represent the local maxima and minima used to identify the timing of the vortex cores.

| AoA | d' | a | h | h/a | h/d' | T triplets | St triplets | T transect | St transect |
[°]	[km]	[km]	[km]	[-]	[-]	[hr]	[-]	[hr]	[-]
16.3 (CC)	11.70	45.83	19.44	0.42	1.66	2.0	0.180	1.7	0.210
0	6.50	32.45	11.07	0.34	1.70	1.3	0.155	1.6	0.127
45	19.78	88.29	37.81	0.43	1.91	4.5	0.140	3.6	0.172
90	23.88	104.49	55.74	0.53	2.34	5.8	0.130	4.6	0.164
-45	16.90	75.33	37.17	0.49	2.20	3.7	0.146	3.3	0.160

Table 2. Vortex street properties

1.66-2.34, and hence slightly higher than the 95% confidence interval found by Young and Zawislak (2006) (1.23-2.00). The Strouhal number obtained with the two procedures are different due to the different computation of T. The values obtained with the Hövmoller diagram tend to be higher. However, the range of variation of St is comparable with the one found in other numerical simulations of AVKVS (Nunalee & Basu, 2014).

Apart from the Strouhal number, the other dimensionless flow parameters defined in Section 2 also change over time. The Reynolds number varies with the upstream wind velocity, u_0, in a range between $4.2 \cdot 10^9$ and $5.4 \cdot 10^9$, while the eddy viscosity Reynolds number, Re_k, varies between a minimum of 2366 and a maximum of 6339. These Re_k values are of the same order of magnitude as the Re numbers based on fluid viscosity and computed on laboratory vortex streets that show features similar to AVKVS. This strengthens the argument of Nunalee and Basu (2014) that adopting the Reynolds number based on eddy viscosity might be useful when deriving the atmospheric analogues of similarity relations obtained for laboratory vortex streets. However, studying non-dimensional parameters and their relationships (such as the St-Re one) is difficult in an unsteady flow and goes beyond the scope of the present work. The Froude number ranges between 0.255-0.434, specifically from 05:00 UTC until the end of the simulations it remains below 0.4, which is the generally recognized condition for the formation of AVKVS (Etling, 1989).

Vortex tracking also allowed the investigation of vorticity decay: peak vorticities were computed for each of the identified vortices and for the five different runs. However, in order to better unveil the differences between the cases and highlight a general trend, instead of plotting individual peak vorticity values, we grouped results according to the distance from the island (data are subdivided in classes of 15 km in width) and then applied a mean filter on vorticity values. The absolute peak vorticity for cyclonic and anticyclonic vortices (red and blue lines, respectively) are plotted in Figure 12. In contrast to the linear trend derived from satellite winds by Horváth et al. (2020) for the control case, we found an exponential decay for all the simulations, which is in better agreement with the decay rate of a classic Kármán vortex street behind a circular cylinder as simulated by Ponta (2010). The plot shows that trailing-edge vortices (i.e., cyclonic ones for all but the -45° case) are characterized by higher peak vorticity than their leading-edge counterparts at the same distance from the island. This difference between positive and negative peak vorticity tends to decrease with increasing angle of attack, as discussed earlier. Note that for AoA = -45° (Figure 12e), the (absolute) peak negative vorticities are the largest ones because the stronger trailing-edge vortices are anticyclonic in this particular case.

The same trends are found when analyzing the mean vorticity of the vortices, as depicted in Figure 13. Similar results have been found in the study of the classical VKVS past an inclined flat plate and can be explained by the already cited vortex formation mechanism postulated by Lam and Leung (2005), causing leading edge vortices to be more diffused and with smaller peak vorticity at the same axial location. This effect decreases

as the angle of attack increases because the streamwise distance between the trailing and leading edge diminishes. Despite the differences between AVKVS and laboratory VKVS formation mechanisms (potential vorticity generation by the deformation of isentropes versus viscous boundary layer separation), our results suggest a fundamental role of leading and trailing edges also for AVKVS features. Indeed, the downstream decay of vorticity in Figure 12 steadily becomes more comparable for cyclonic and anticyclonic vortices as α increases. The effect of Earth's rotation is superimposed on this mechanism, enhancing cyclonic vortices and inhibiting anticyclonic ones. However, when the direction of rotation of trailing and leading edge vortices is swapped as in the case of $\alpha = -45°$, as suggested from (Figure 12e), the anticyclonic trailing-edge vortices display larger absolute vorticity values than the cyclonic leading-edge vortices, despite the Coriolis effect's strengthening of cyclonic rotation. This suggests that the asymmetry of island shape relative to the incident flow is the dominant factor controlling the asymmetry of the vortex street for $\alpha < 90°$. For $\alpha = 90°$, the shape effect mostly disappears, and the Coriolis effect alone leads to slightly stronger cyclonic vortices in the northern hemisphere (Figure 12d and Figure 13d).

As mentioned earlier, vortex size also depends on AoA due to corresponding variations in the crosswind island diameter. To better highlight this issue, we determined the size of vortices when they crossed the section used for the Hövmoller diagrams. At such a small downstream distance from the island, the widening due to diffusion and the consequent uncertainty in vortex boundary identification is relatively small. Figure 14 shows the vortex equivalent diameter d_{eq} (i.e. the diameter of the circle with the same area) as a function of the crosswind island diameter, d': the different symbols represent different AoAs, while red and blue colours mark cyclonic and anticyclonic vortices, respectively. The results clearly show that cyclonic vortices tend to be larger (except for $\alpha = -45°$), and vortex size steadily increases with the obstacle diameter d'. Equivalent diameters obtained for positive α values (16°, 45° and 90°) follow a linear increase, and a roughly constant difference is present between cyclonic and anticyclonic vortex size. When the island is parallel with the incoming flow ($\alpha = 0°$), vortices of the opposite signs have approximately the same size. However, this estimate is quite uncertain since there is only one anticyclonic vortex in this case.

Considering the case with $\alpha = -45°$, one might expect a reversal in the relative size of the vortices compared to the case with $\alpha = 45°$, that is, larger anticyclonic vortices than cyclonic ones. The results instead show vortices of different rotations having a similar size. This might be due to the Coriolis effect, which weakens the anticyclonic vortices in the northern hemisphere. An investigation of the Coriolis effects goes beyond the scope of the present paper and will be addressed in a follow-up work. In addition, for $\alpha = 45°$ the footprints of the vortices are generally larger and more diffuse than for $\alpha = -45°$ (cf. Figure 8c and Figure 9c). We also note that the angle of attack is computed relative to the average wind direction, and the d' for the two runs is comparable but not exactly the same; hence, the two configurations are not perfectly mirrored.

5 Conclusions

Mesoscale meteorological simulations performed with the WRF model were used to evaluate the role of the angle of attack in the development of atmospheric von Kármán vortex streets. The AVKVS that occurred in the lee of Guadalupe on 9 May 2018 was simulated and assumed as a control case, while different runs with the same synoptic conditions were performed with rotated island topography. A vortex tracking procedure allowed for deriving geometrical parameters, such as the aspect ratio of the vortices, which were generally in line with those analyzed by Young and Zawislak (2006) and retrieved from MODIS images of island wakes. The crosswind island diameter was confirmed to be the characteristic length of the obstacle that determines the size of the shed vortices. The analysis of peak vorticity decay revealed that wake asymmetry decreases with in-
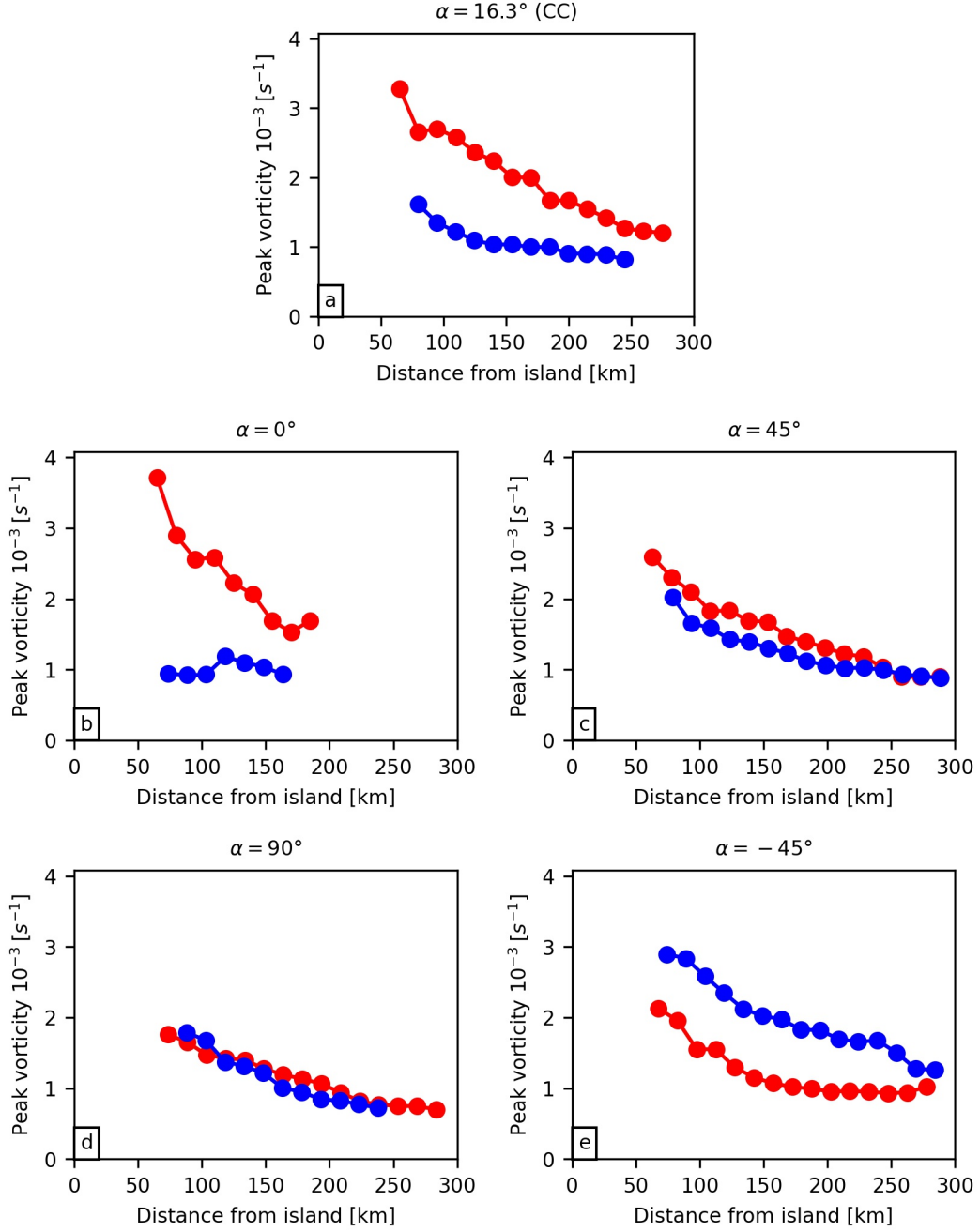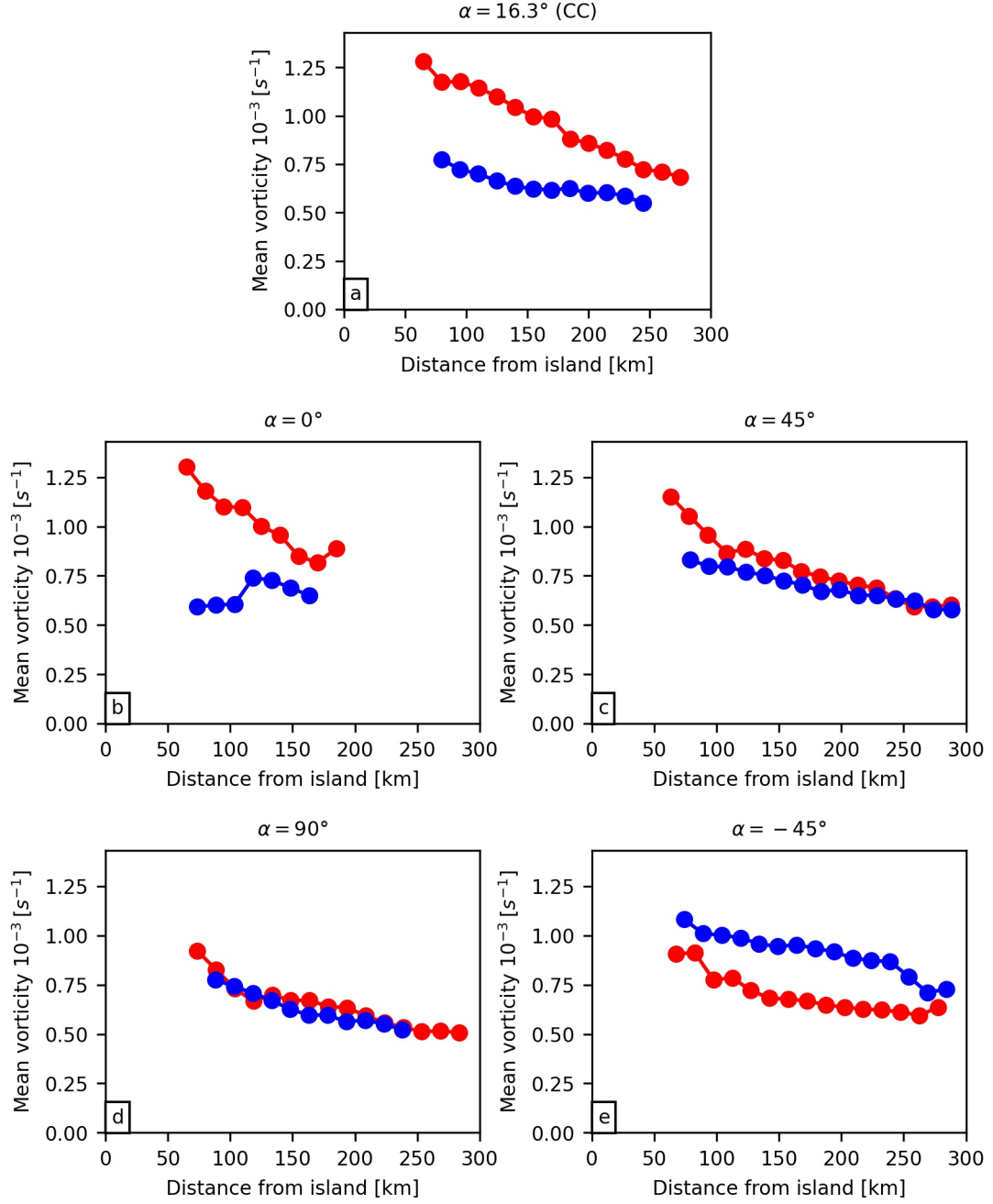
Figure 12.   The absolute value of peak vorticity of cyclonic (red) and anticyclonic (blue) vortices plotted versus their distance from the island. Vorticity decay for the five different cases: control case (panel a) and the island rotations corresponding to $\alpha =$ to 0°, 45°, 90° and -45° (panels b,c,d, and e, respectively).
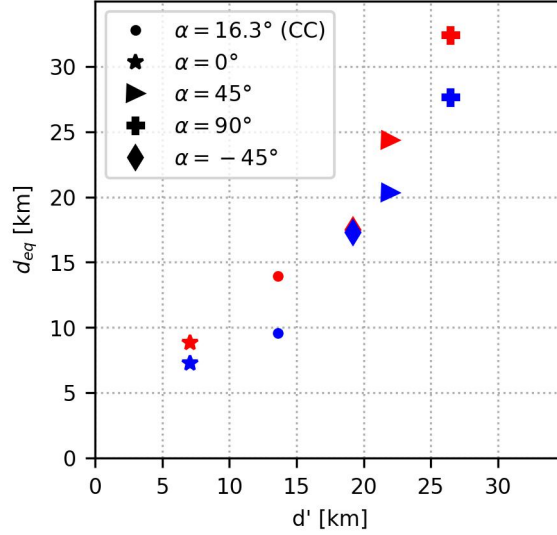
Figure 13. The absolute value of mean vorticity of cyclonic (red) and anticyclonic (blue) vortices plotted versus their distance from the island. Vorticity decay for the five different cases: control case (panel a) and the island rotations corresponding to $\alpha =$ to 0°, 45°, 90° and -45° (panels b,c,d, and e,respectively).

Figure 14. Equivalent diameter, d_{eq}, of cyclonic (red) and anticyclonic (blue) vortices versus obstacle cross-stream diameter, d' for the five model runs.

creasing angle of attack. We also found that the asymmetry is fundamentally between trailing-edge and leading-edge vortices rather than between cyclonic and anticyclonic vortices. Under the typical conditions of northwesterly flow relative to the island's major axis, the stronger trailing-edge vortices are cyclonic. However, when the rotated orientation of the island mimics northeasterly flow, the anticyclonic vortices are stronger because they are the trailing-edge ones. The switch to stronger anticyclonic vortices occurs despite the Coriolis effect selectively strengthening cyclonic vortices. This result suggests that the role of an elongated island shape is at least comparable to that of earth's rotation in modulating the wake asymmetry. Our future work will systematically analyze and quantify the effect of the Coriolis force on AVKVS development. To obtain more general results, independent of the specifics of Guadalupe's topography, a similar analysis can be performed for an idealized elliptic-shaped island.

Data Availability Statement

The hourly ERA5 data used in this study as initial and boundary conditions are available at the website https://cds.climate.copernicus.eu/ (doi: https://doi.org/10.24381/cds.bd0915c6 for data on pressure levels, and https://doi.org/10.24381/cds.adbb2d47 for data on single level). The GMTED2010 dataset used for the simulations is available from the website https://www.usgs.gov/coastal-changes-and-impacts (doi: https://doi.org/10.5066/F7J38R2N). The satellite images used for the comparison are available at the website https://worldview.earthdata.nasa.gov/. The setup for the WRF simulations, the code to rotate Guadalupe island, and the code and data used to plot the Figure 3 are available from the Zenodo data repository (https://doi.org/10.5281/zenodo

References

Breuer, M., & Jovičić, N. (2001). Separated flow around a flat plate at high incidence: An LES investigation. *Journal of Turbulence*, *2*, 18-. doi: https://doi.org/10.1088/1468-5248/2/1/018

Caldeira, R. M. A., & Tomé, R. (2013). Wake response to an ocean-feedback mechanism: Madeira Island case study. *Boundary-Layer Meteorology*, *148*(2), 419–436. doi: https://doi.org/10.1007/s10546-013-9817-y

Chen, F., & Dudhia, J. (2001). Coupling an advanced land surface–hydrology model with the Penn State–NCAR MM5 modeling system. part i: Model implementation and sensitivity. *Monthly Weather Review*, *129*, 569-585. doi: https://doi.org/10.1175/1520-0493(2001)129⟨0569:CAALSH⟩2.0.CO;2

Chopra, K. P., & Hubert, L. F. (1965). Mesoscale eddies in wake of islands. *Journal of Atmospheric Sciences*, *22*(6), 652 - 657. doi: https://doi.org/10.1175/1520-0469(1965)022"⟨"0652:MEIWOI⟩2.0.CO;2

Couvelard, X., Caldeira, R., Araujo, I., & Tomé, R. (2012, 11). Wind mediated vorticity-generation and eddy-confinement, leeward of the Madeira Island: 2008 numerical case study. *Dynamics of Atmospheres and Oceans*, *58*, 128–149. doi: https://doi.org/10.1016/j.dynatmoce.2012.09.005

Danielson, J. J., & Gesch, D. B. (2011). *Global multi-resolution terrain elevation data 2010 (GMTED2010)*. U.S. Geological Survey. doi: https://doi.org/10.3133/ofr20111073

Etling, D. (1989). On atmospheric vortex streets in the wake of large islands. *Meteorology and Atmospheric Physics*, *41*(3), 157–164. doi: https://doi.org/10.1007/BF01043134

Etling, D. (1990). Mesoscale vortex shedding from large islands: A comparison with laboratory experiments of rotating stratified flows. *Meteorology and Atmospheric Physics*, *43*(1-4), 145-151. doi: https://doi.org/10.1007/BF01028117

Fage, A., Johansen, F. C., & Lamb, H. (1927). On the flow of air behind an inclined flat plate of infinite span. *Proceedings of the Royal Society of London. Series A, Containing Papers of a Mathematical and Physical Character*, *116*(773), 170-197. doi: https://doi.org/10.1098/rspa.1927.0130

Gao, Q., Zeman, C., Vergara-Temprado, J., Lima, D. C. A., Molnar, P., & Schär, C. (2023). Vortex streets to the lee of Madeira in a kilometre-resolution regional climate model. *Weather and Climate Dynamics*, *4*(1), 189–211. doi: https://doi.org/10.5194/wcd-4-189-2023

Grubišić, V., Sachsperger, J., & Caldeira, R. M. A. (2015). Atmospheric wake of Madeira: First aerial observations and numerical simulations. *Journal of the Atmospheric Sciences*, *72*(12), 4755–4776. doi: https://doi.org/10.1175/JAS-D-14-0251.1

Günther, T., Horváth, A., Bresky, W., Daniels, J., & Buehler, S. A. (2021). Lagrangian coherent structures and vortex formation in high spatiotemporal-resolution satellite winds of an atmospheric Kármán vortex street. *Journal of Geophysical Research: Atmospheres*, *126*. doi: https://doi.org/10.1029/2021JD035000

Heinze, R., Raasch, S., & Etling, D. (2012). The structure of Kármán vortex streets in the atmospheric boundary layer derived from large eddy simulation. *Meteorologische Zeitschrift*, *21*(3), 221–237. doi: https://doi.org/10.1127/0941-2948/2012/0313

Hersbach, H., Bell, B., Berrisford, P., Hirahara, S., Horányi, A., Muñoz-Sabater, J., ... Thépaut, J. (2020). The ERA5 global reanalysis. *Quarterly Journal of the Royal Meteorological Society*, *146*(730), 1999–2049. doi: https://doi.org/10.1002/qj.3803

Hong, S.-Y., Dudhia, J., & Chen, S.-H. (2004). A revised approach to ice microphysical processes for the bulk parameterization of clouds and precipitation. *Monthly Weather Review*, *132*(1), 103–120. doi: https://doi.org/10.1175/

1520-0493(2004)132⟨0103:ARATIM⟩2.0.CO;2

Horváth, A., Bresky, W., Daniels, J., Vogelzang, J., Stoffelen, A., Carr, J., . . . Buehler, S. (2020). Evolution of an atmospheric Kármán vortex street from high-resolution satellite winds: Guadalupe Island case study. *Journal of Geophysical Research: Atmospheres*, *125*(4). doi: https://doi.org/10.1029/2019JD032121

Hubert, L. F., & Krueger, A. F. (1962). Satellite pictures of mesoscale eddies. *Monthly Weather Review*, *90*(11), 457 - 463. doi: https://doi.org/10.1175/1520-0493(1962)090⟨0457:SPOME⟩2.0.CO;2

Iacono, M. J., Delamere, J. S., Mlawer, E. J., Shephard, M. W., Clough, S. A., & Collins, W. D. (2008). Radiative forcing by long-lived greenhouse gases: Calculations with the aer radiative transfer models. *Journal of Geophysical Research: Atmospheres*, *113*(D13). doi: https://doi.org/10.1029/2008JD009944

Ito, J., & Niino, H. (2016). Atmospheric Kármán vortex shedding from Jeju Island, East China Sea: A numerical study. *Monthly Weather Review*, *144*(1), 139–148. doi: https://doi.org/10.1175/MWR-D-14-00406.1

Jiménez, P. A., Dudhia, J., González-Rouco, J. F., Navarro, J., Montávez, J. P., & García-Bustamante, E. (2012). A revised scheme for the WRF surface layer formulation. *Monthly Weather Review*, *140*(3), 898–918. doi: https://doi.org/10.1175/MWR-D-11-00056.1

Kain, J. S. (2004). The Kain–Fritsch convective parameterization: An update. *Journal of Applied Meteorology*, *43*(1), 170–181. doi: https://doi.org/10.1175/1520-0450(2004)043⟨0170:TKCPAU⟩2.0.CO;2

Karmán, T. v. (1912). Über den mechanismus des wiederstandes, den ein bewegter korper in einer flüssigkeit erfahrt. *Nachrichten von der Gesellschaft der Wissenschaften zu Göttingen, Mathematisch-Physikalische Klasse*, *1912*, 547-556.

Kármán, T. v. (1911). Ueber den mechanismus des widerstandes, den ein bewegter körper in einer flüssigkeit erfährt. *Nachrichten von der Gesellschaft der Wissenschaften zu Göttingen, Mathematisch-Physikalische Klasse*, *1911*, 509-517.

Lam, K. (1996). Phase-locked eduction of vortex shedding in flow past an inclined flat plate. *Physics of Fluids*, *8*, 1159-1168. doi: https://doi.org/10.1063/1.868907

Lam, K., & Leung, M. (2005). Asymmetric vortex shedding flow past an inclined flat plate at high incidence. *European Journal of Mechanics B-fluids*, *24*, 33-48. doi: https://doi.org/10.1016/j.euromechflu.2004.05.004

Lam, K., & Wei, C. (2010). Numerical simulation of vortex shedding from an inclined flat plate. *Engineering Applications of Computational Fluid Mechanics*, *4*(4), 569–579. doi: https://doi.org/10.1080/19942060.2010.11015342

Li, S., Jaroszynski, S., Pearse, S., Orf, L., & Clyne, J. (2019, 08). Vapor: A visualization package tailored to analyze simulation data in earth system science. *Atmosphere*, *10*, 488. doi: https://doi.org/10.3390/atmos10090488

Li, X., Zheng, W., Zou, C.-Z., & Pichel, W. (2008). A SAR observation and numerical study on ocean surface imprints of atmospheric vortex streets. *Sensors*, *8*(5), 3321–3334. doi: https://doi.org/10.3390/s8053321

Nakanishi, M., & Niino, H. (2004). An improved Mellor–Yamada level-3 model with condensation physics: its design and verification. *Boundary-Layer Meteorology*, *112*(1), 1–31. doi: https://doi.org/10.1023/B:BOUN.0000020164.04146.98

Nunalee, C. G., & Basu, S. (2014). On the periodicity of atmospheric von Kármán vortex streets. *Environmental Fluid Mechanics*, *14*(6), 1335–1355. doi: https://doi.org/10.1007/s10652-014-9340-9

Nunalee, C. G., He, P., Basu, S., Minet, J., & Vorontsov, M. A. (2015). Mapping optical ray trajectories through island wake vortices. *Meteorology and Atmospheric Physics*, *127*(3), 355–368. doi: https://doi.org/10.1007/s00703-015-0366-4

Nunalee, C. G., Horváth, A., & Basu, S. (2015). High-resolution numerical modeling

of mesoscale island wakes and sensitivity to static topographic relief data. *Geoscientific Model Development*, *8*, 2645–2653. doi: https://doi.org/10.5194/gmd-8-2645-2015

Ponta, F. (2010). Vortex decay in the Kármán eddy street. *Physics of Fluids*, *22*. doi: https://doi.org/10.1063/1.3481383

Skamarock, W. C., Klemp, J. B., Dudhia, J., Gill, D. O., Barker, D. M., Duda, G. D., . . . Powers, J. G. (2008). A description of the Advanced Research WRF version 3. doi: https://doi.org/10.5065/D68S4MVH

Snyder, W., Thompson, R., Eskridge, R., Lawson, R., Castro, I., Lee, J., . . . Ogawa, Y. (1985). The structure of strongly stratified flow over hills: dividing-streamline concept. *Journal of Fluid Mechanics*, 249. doi: https://doi.org/10.1017/S0022112085000684

Yang, D., Pettersen, B., Andersson, H., & Narasimhamurthy, V. (2012). Vortex shedding in flow past an inclined flat plate at high incidence. *Physics of Fluids*, *24*. doi: https://doi.org/10.1063/1.4744982

Young, G. S., & Zawislak, J. (2006). An observational study of vortex spacing in island wake vortex streets. *Monthly Weather Review*, *134*(8), 2285–2294. doi: https://doi.org/10.1175/MWR3186.1

Ágústsson, H., & Ólafsson, H. (2014). The advection of mesoscale atmospheric vortices over Reykjavík. *Monthly Weather Review*, *142*(10), 3549 - 3559. doi: https://doi.org/10.1175/MWR-D-13-00060.1